Characterization of precipitating clouds by ground-based measurements with the triple-frequency polarized Microwave Radiometer ADMIRARI

Original

Characterization of precipitating clouds by ground-based measurements with the triple-frequency polarized Microwave Radiometer ADMIRARI / Battaglia, A., Saavedra, P., Rose, T., Simmer, C.. - In: JOURNAL OF APPLIED METEOROLOGY AND CLIMATOLOGY. - ISSN 1558-8424. - 49:3(2010), pp. 394-414. [10.1175/2009JAMC2340.1]

Publisher:

AMER METEOROLOGICAL SOC

Published

DOI:10.1175/2009JAMC2340.1

Characterization of Precipitating Clouds by Ground-Based Measurements with the Triple-Frequency Polarized Microwave Radiometer ADMIRARI

ALESSANDRO BATTAGLIA AND PABLO SAAVEDRA

Meteorological Institute, University of Bonn, Bonn, Germany

THOMAS ROSE

Radiometer Physics GmbH, Meckenheim, Germany

CLEMENS SIMMER

Meteorological Institute, University of Bonn, Bonn, Germany

(Manuscript received 30 June 2009, in final form 18 September 2009)

ABSTRACT

A groundbreaking new-concept multiwavelength dual-polarized Advanced Microwave Radiometer for Rain Identification (ADMIRARI) has been built and continuously operated in two field campaigns: the Convective and Orographically Induced Precipitation Study (COPS) and the European Integrated Project on Aerosol Cloud Climate Air Quality Interactions (EUCAARI). The radiometer has 6 channels working in horizontal and vertical polarization at 10.65, 21.0, and 36.5 GHz, and it is completely steerable both in azimuth and in elevation. The instrument is suited to be operated in rainy conditions and is intended for retrieving simultaneously water vapor, rain, and cloud liquid water paths. To this goal the authors implemented a Bayesian retrieval scheme based on many state realizations simulated by the Goddard Cumulus Ensemble model that build up a prior probability density function of rainfall profiles. Detailed three-dimensional radiative transfer calculations, which account for the presence of nonspherical particles in preferential orientation, simulate the downwelling brightness temperatures and establish the similarity of radiative signatures and thus the probability that a given profile is actually observed. Particular attention is devoted to the sensitivity of the ADMIRARI signal to 3D effects, raindrop size distribution, and axial ratio parameterizations. The polarization and multifrequency signals represent key information to separate the effects introduced by non-Rayleigh scatterers and to separate rainwater (r-LWP) from the cloud water component (c-LWP). Long-term observations demonstrate that observed brightness temperatures and polarization differences can be well interpreted and reproduced by the simulated ones for all three channels simultaneously. Rough estimates of r-LWP derived from collocated observations with a micro rain radar confirm the rain/no rain separation and the variability trend of r-LWP provided by the radiometer-based retrieval algorithm. With this work the authors demonstrate the potential of ADMIRARI to retrieve information about the rain/cloud partitioning for midlatitude precipitation systems; future studies with this instrument will provide crucial information on rain efficiency of clouds for cloud modelers that might lead toward a better characterization of rain processes.

1. Introduction

Ground-based microwave (MW) radiometry is a fairly established technique to retrieve vertically integrated cloud liquid water path (c-LWP) with dual-channel radiometers (see Westwater 1978; Liljegren et al. 2001; Crewell and Löhnert 2003; Westwater et al. 2004; Rose et al. 2005) and water vapor and temperature profiles with multifrequency radiometers (see Solheim et al. 1998; Janssen 1996; Crewell et al. 2001; Löhnert et al. 2008, 2009). Ground-based observations are known to be the most accurate method to observe total liquid water path (LWP) of optically thick clouds with an estimated accuracy of up to 15 g m^{-2} (Crewell and Löhnert 2003). Above about 300 g m^{-2}, however, clouds

---

Corresponding author address: Alessandro Battaglia, Meteorological Institute, University of Bonn, Auf dem Huegel 20, D-53121 Bonn, Germany.
E-mail: batta@uni-bonn.de

DOI: 10.1175/2009JAMC2340.1

generally contain raindrops that have the following characteristics:

(i) The raindrops may wet the receiving antenna, thus producing absorption losses directly at the antenna window or at the reflector plate used to redirect the radiation into the radiometer feed window. The contamination affects the observed brightness temperatures (T_Bs) to an extent that depends on rain rate, design of the radiometer, and frequency of operation (Jacobson et al. 1986).

(ii) The raindrops limit the applicability of the Rayleigh approximation, according to which the extinction coefficient is proportional to the mass of the particles so that the total optical thickness is directly proportional to the total LWP. Cloud droplets produce a different mass extinction coefficient than raindrops because in the Mie-resonance region (for the specific application size parameters are always lower than 3) the extinction cross sections remain above their Rayleigh counterparts. Therefore, the same LWP appears "brighter" (i.e., produces higher T_Bs) when the rain component is predominant. For instance, Czekala et al. (2001b) showed that a 1-km-thick cloud containing a total LWP of 1 kg m^{-2} with different rain/cloud partitioning can produce T_Bs in the range 60–130 K when observed by a ground-based radiometer looking at 30° elevation angle. Similar results are presented in section 3 of Sheppard (1996).

As a direct implication, in LWP retrieval the RMS and bias errors strongly increase in presence of rain and can easily rise above 100 g m^{-2} even for total LWP less than 1 kg m^{-2} (see section 5 in Löhnert and Crewell 2003 and section 4 in Sheppard 1996).

The first issue has been addressed by using either spinning reflectors (Jacobson and Nunnelee 1997) or shutters connected to rain sensors (Crewell et al. 2001), by introducing hydrophobic coatings on the antennas (Marzano et al. 2005b), or by adopting a combination of slant viewing angle configuration and fans (Liu et al. 2001). To relieve the second limitation and to resolve the ambiguity introduced by raindrops, two main methodologies have been proposed.

a. *Polarization studies*

Czekala et al. (2001b) suggested measuring the polarization signal PD $\equiv T_B^V - T_B^H$, which is related to the raindrop size. Large raindrops have nonspherical shapes because of surface tension, internal hydrostatic pressure and friction stress (e.g., Chuang and Beard 1990). They can be modeled, on average, as oblate spheroids with axial ratio lower than one (parameterizations provided by, e.g., Andsager et al. 1999). Radiative transfer computations performed by Czekala and Simmer (1998) have shown that T_Bs are only marginally affected by raindrop shape, while the polarization differences (PDs) are strongly influenced by it. In particular, for downwelling radiation [for upwelling radiation (satellite view) the signal is less interpretable because of interferences by variable ice particle amounts; e.g., Czekala and Simmer 2002], the PDs change from small positive values (when spherical raindrops are considered; see, e.g., Liu and Simmer 1996) to large negative values in case of nonspherical particles. The polarization signal can therefore be adopted as a strong signature of the presence of raindrops and can help in the discrimination between c-LWP and rain liquid water path (r-LWP).

Few ground-based polarized measurements at MW frequencies have been documented in literature, like those performed with a 19.2-GHz dual-polarization radiometer at 30° elevation angle in southern Germany during 5 months in 1996 and continuously from November 1998 to December 1999 (see Czekala et al. 2001a for details). The mean PD observations (with corresponding standard deviation) sorted according to the T_B values show a typical signal: the PD decreases first to negative values with increasing T_B; then the PD saturates at its largest negative values around T_Bs of 200 K and finally increases back toward 0 for $T_B > 220$ K. The same authors showed that, in order to explain these signatures, it is necessary to introduce nonspherical partially oriented raindrops. Although the acquired dataset is quite large (513 observation days), the lack of other remote sensing instruments at the measurement site was a major obstacle for the conclusive interpretation of the results.

Similar measurements but of much smaller extent have been presented already by Kutuza et al. (1998), who also confirmed the presence of negative polarization in rain. Troitsky et al. (2003) have analyzed data acquired by a two-frequency (85 and 37 GHz) dual-polarized ground-based radiometer looking at a zenith angle of 65° during the Alliance Icing Research Project held in Ottawa in the winter 1999/2000. Their observations refer, however, to snowy condition and are more suited for mixed-phase hydrometeor studies. In their study, the polarization signatures are related to the ice water path and to the microphysics of crystal particles and not to the differential emission–absorption typical of raindrops.

b. *Multispectral studies*

Other authors (Sheppard 1996; Liu et al. 2001; Marzano et al. 2002, 2005a, 2006; Mätzler and Morland 2008) have focused on the potential of multiwavelength ground-based radiometer observations in retrieving integrated rain contents of precipitating clouds. Sheppard (1996) showed agreement between radiometric measurements at 20, 31, and 52 GHz and model computations with a standard error around 4–7 K. Liu et al. (2001) used a dual-frequency system (19–22 GHz) with a very poor angular resolution (25°) and showed that for this setup one hour is the optimal averaging period when comparing radiometric-derived and gauge-measured rain rates. Marzano et al. (2002, 2005a, 2006) developed different physically based retrieval algorithms (based on multiple regression, on a statistical inversion driven by a principal component analyses, and on a neural network approach, respectively), applied them to different combinations of multifrequency ground-based measurements, and compared these with rain gauge data (they used typically 30-min accumulated values). Such comparisons are, however, plagued by the internal weakness that the atmospheric opacity structure coupled with the nonlinearity of the radiation signal has a vastly different temporal and spatial scale than the point like and time-integrated gauge data. Marzano et al. (2006) therefore presented a more favorable comparison between rain path attenuation directly derived from the 18.7-, 39.6-, and 49.5-GHz Italy and Communication Satellite System (ITALSAT) beacons and the rain amounts retrieved from ground-based radiometric measurements at 13.0, 23.8, and 31.6 GHz.

Mätzler and Morland (2008) exploited the 31-GHz channel of the Tropospheric Water Vapor Radiometer (TROWARA) to derive rain rates directly from the retrieved optical thickness at this frequency, by using constraints on the rain column height derived from radiosonde measurements and the opacity of the atmosphere without rain with the help of other radiometric channels.

The Advanced Microwave Radiometer for Rain Identification (ADMIRARI) has been developed to provide a bridge between the multispectral and the polarimetric approach, to evaluate the additional information content of polarization differences, and to assess the accuracy requirements needed for such measurements. The central goal of ADMIRARI observations is a better characterization of the state of the atmosphere in rainy conditions, with a particular emphasis on the cloud–rain partitioning. An improvement in the quantitative monitoring of a rainy atmosphere has important repercussions in many fields, for example, in validating the assumed efficiency of cloud to rain conversion in cloud modeling (see introduction in Battaglia et al. 2009) or in better estimating the effect of the cloud attenuation for high-frequency radars (Pujol et al. 2007).

After describing the ADMIRARI design (section 2) and presenting an example of its measurements performed during field campaigns in section 3, the modeling of the ADMIRARI signal is presented in section 4 via detailed 3D polarized radiative transfer simulations. The Bayesian retrieval algorithm is discussed and exemplified in section 5. Conclusions are drawn and future work is discussed in section 6.

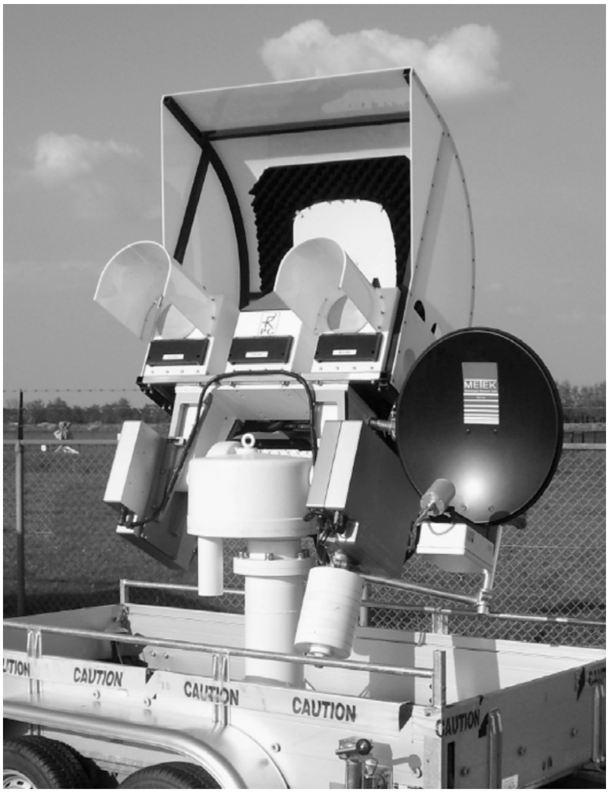

FIG. 1. The ADMIRARI radiometer at the Cabauw Experimental Site for Atmospheric Research (CESAR) observatory. On the right side (black antenna) a micro rain radar system is installed.

2. Description of the ADMIRARI radiometer

ADMIRARI (see picture in Fig. 1), manufactured by Radiometer Physics GmbH, has been designed to investigate rain processes. The main instrument characteristics are summarized in Table 1. Additional information can also be found at the ADMIRARI home page (http://www.meteo.uni-bonn.de/forschung/gruppen/admirari/).

The standard atmospheric parameters, which can be derived from ADMIRARI observations, are c-LWP, r-LWP, and the integrated water vapor (IWV). For this purpose the radiometer comprises in total six channels covering three frequencies (10.65, 21.0, and 36.5 GHz) and both linear polarizations (H and V). These frequencies have been selected based on different considerations:

- The use of a multifrequency approach allows a better discrimination of different rain-rate classes. For

TABLE 1. Main characteristics of the ADMIRARI radiometer.

Feature	Specification
Center frequencies (GHz)	10.65–21.0–36.5
Bandwidth (MHz)	400
Min integration time (s)	1
System noise temperature	<900 K for all receivers
Absolute system stability	1.0 K
Receiver and antenna thermal stabilization	Accuracy <0.05 K
Antenna beamwidth	5°−6.5°−6.5°
Side lobes	<-35 dB*c* <-40 dB*c* <-40 dB*c*
Cross polarization	<-20 dB
Pointing speed	Elev: 3° s^{-1}; azimuth: 5° s^{-1}

instance, the sensitivity to small amounts of r-LWP is significantly better at the higher frequency (see Figs. 2–3 in Czekala et al. 2001b), while high amounts are better monitored at the lower frequency.

- The radiometer must produce the usual dual-channel IWV–LWP product for no-rain conditions. Therefore one frequency, −21.0 GHz, with weighting function almost independent of height, has been selected within the weak 22-GHz water vapor absorption line and the other (36.5 GHz) in the window region between this line and the oxygen line complex around 60 GHz.
- The three ADMIRARI frequencies mirror those that are/will be present in many spaceborne radiometers [e.g., Tropical Rainfall Measuring Mission (TRMM) Microwave Imager (TMI), Special Sensor Microwave Imager (SSM/I), and Global Precipitation Measurement (GPM) Microwave Imager (GMI)]. Thus this setup offers an important contribution to the ground-based observations that can be used to validate passive microwave spaceborne rain-rate retrieval algorithms.

The general radiometer configuration is illustrated in Fig. 2. For each frequency module the receiver optics consists of a corrugated feed horn with an aperture lens (at 10.65 GHz the beam is formed by a combination of a corrugated feed horn and an off-axis parabola antenna), which achieves an antenna beamwidth of approximately 5°. The aperture lenses and the 10-GHz parabola antenna are coated by a water-repellent film to prevent raindrops from sticking to them; they are also equipped with a shield that is effective in protecting the lenses and the parabola antenna from rain when the radiometer is measuring at low elevation angles (typically 20°–40°). These angles are favorably affecting the polarization signal as well (see discussion in section 4) and have been selected for normal operation. In only a few cases have we experienced antenna wetting, for situations with strong wind blowing toward the radiometer viewing direction. In the absence of ''adverse'' wind, observations with elevation angles up to 60° are generally not affected by antenna wetting. To undoubtedly confirm the antennas dryness during operation, we are now planning to install antenna-monitoring video cameras.

The corrugated feed horns offer a low cross-polarization level and a rotationally symmetric beam pattern. The orthomode transducer splits the signal into the V and H polarization components. The ADMIRARI receivers are designed to achieve a high thermal and electrical stability, a compact layout with a minimum of connectors and thermally drifting components, an integrated radiofrequency design, and low power consumption and weight. The receivers are based on the direct detection technique (thus no mixers and local oscillators are needed, leading to reduced sensitivity to interfering external signals at down-converted frequencies). As illustrated in the bottom panel of Fig. 2, a Dicke switch periodically switches the receiver inputs to an internal blackbody with fixed T_B. In combination with the built-in noise injection system, the radiometer automatically performs a continuous calibration of all relevant drift parameters like gain and system noise temperature. The Dicke switches are wide-bandwidth Y-junction circulators where one port is terminated by absorber material. By inverting the magnetic field direction, the isolator function of this device is also reverted. When the radiometer is ''looking'' to the sky, its input is isolated from all signals coming from the receiver input (e.g., the noise power reflected from the noise injection system). When the Dicke switch is in the ''on'' state, the receiver input is isolated from signals coming from the sky. The Dicke switch is followed by a directional coupler that allows for the injection of a precision noise signal generated by an on/off switching calibrated noise source. This noise signal is used to determine system nonlinearities and system gain drifts during measurements by the ''four point'' method (Crewell et al. 2001, Fig. 9). A 40-dB low noise amplifier (LNA) boosts the input signal before it is filtered by a waveguide bandpass filter with bandwidth 200 MHz and again boosted by another 20-dB amplifier. Each of the six channels has its own detector diode, which allows for a parallel detection and integration. The detector outputs are finally amplified by an ultralow drift operational amplifier chain, analog–digital converted, and transmitted to the internal radiometer personal computer for each of the three frequency modules.

To fulfill the requirement of low maintenance regarding absolute calibrations, the receivers are integrated together with their feeds and lenses and are thermally insulated to achieve a high thermal stability with an accuracy of <0.05 K over the whole operating temperature range (from −30° to +40°C). The system achieves

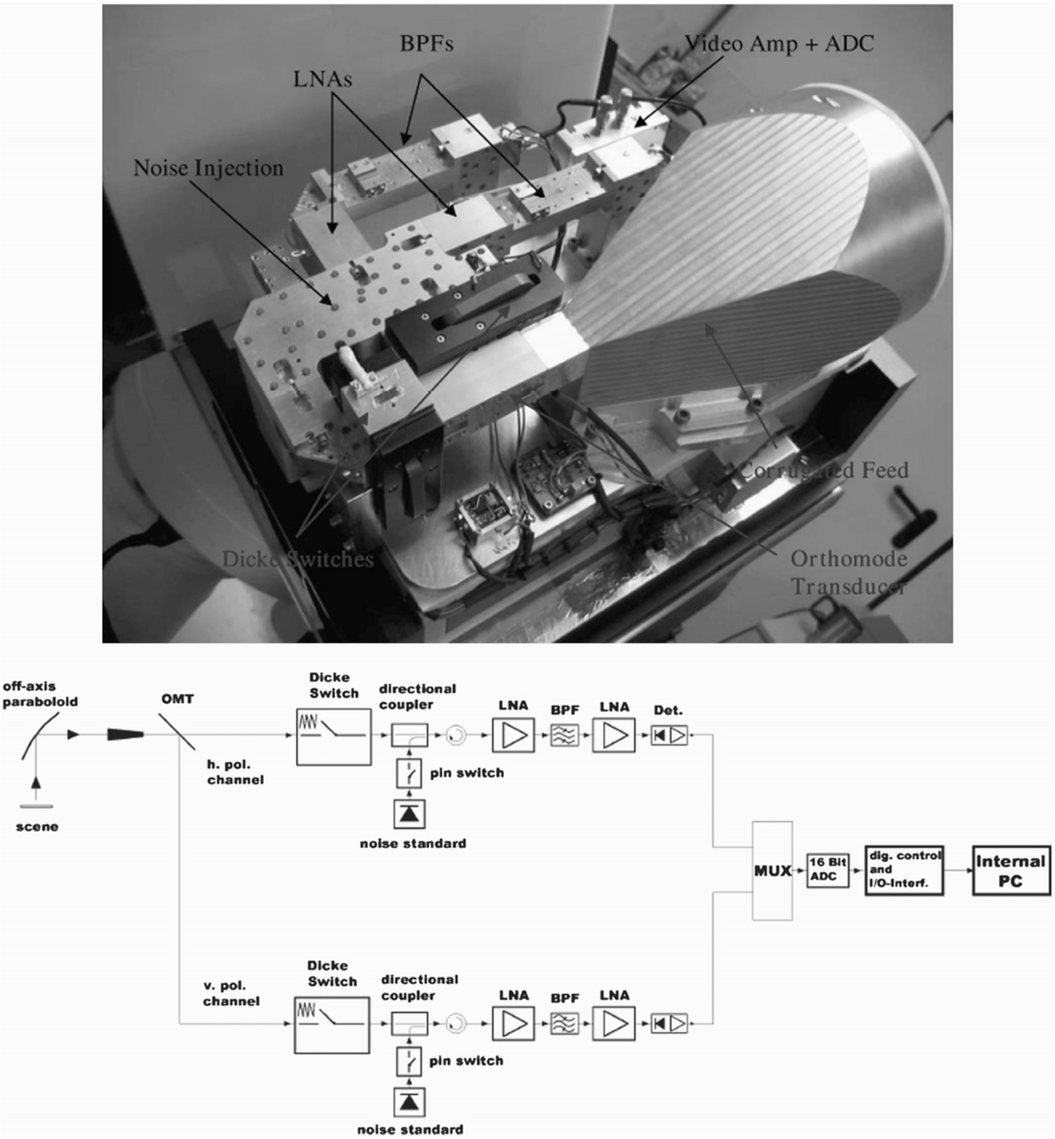

FIG. 2. (top) Picture of the inner radiometer components and (bottom) a schematic of the receiver layout. The orthomode transducer is splitting the *H* and *V* signals, which are directly detected in two different receiving chains.

a full internal calibration by using the internal Dicke switch calibration targets (absolute standards) in combination with the built-in noise injection systems (one for each frequency module), which are used to calibrate the gain drifts. Noise diodes are secondary standards; they are calibrated by sky-tipping procedures, which can be manually performed during clear-sky conditions. A radiometer resolution lower than 0.4 K RMS at 1.0-s integration time is achieved with an absolute system stability of 1.0 K. The system is fully steerable both in azimuth (0°–360°) and in zenith (from −90° to +90°) with azimuthal speed and elevation speed approximately equal to 5° and 3° s^{-1}, respectively. To allow easy transportation to campaign sites, the whole system is mounted on a trailer (Fig. 1).

3. COPS and EUCAARI campaign

During its first life year, ADMIRARI has participated in the Convective and Orographically induced Precipitation Study (COPS; Wulfmeyer et al. 2008) and in the European Integrated Project on Aerosol Cloud Climate Air Quality Interactions (EUCAARI) campaign (www.knmi.nl/eucaari/). Measurements obtained during the COPS campaign were already reported in Battaglia et al. (2009). After this first campaign the radiometer design

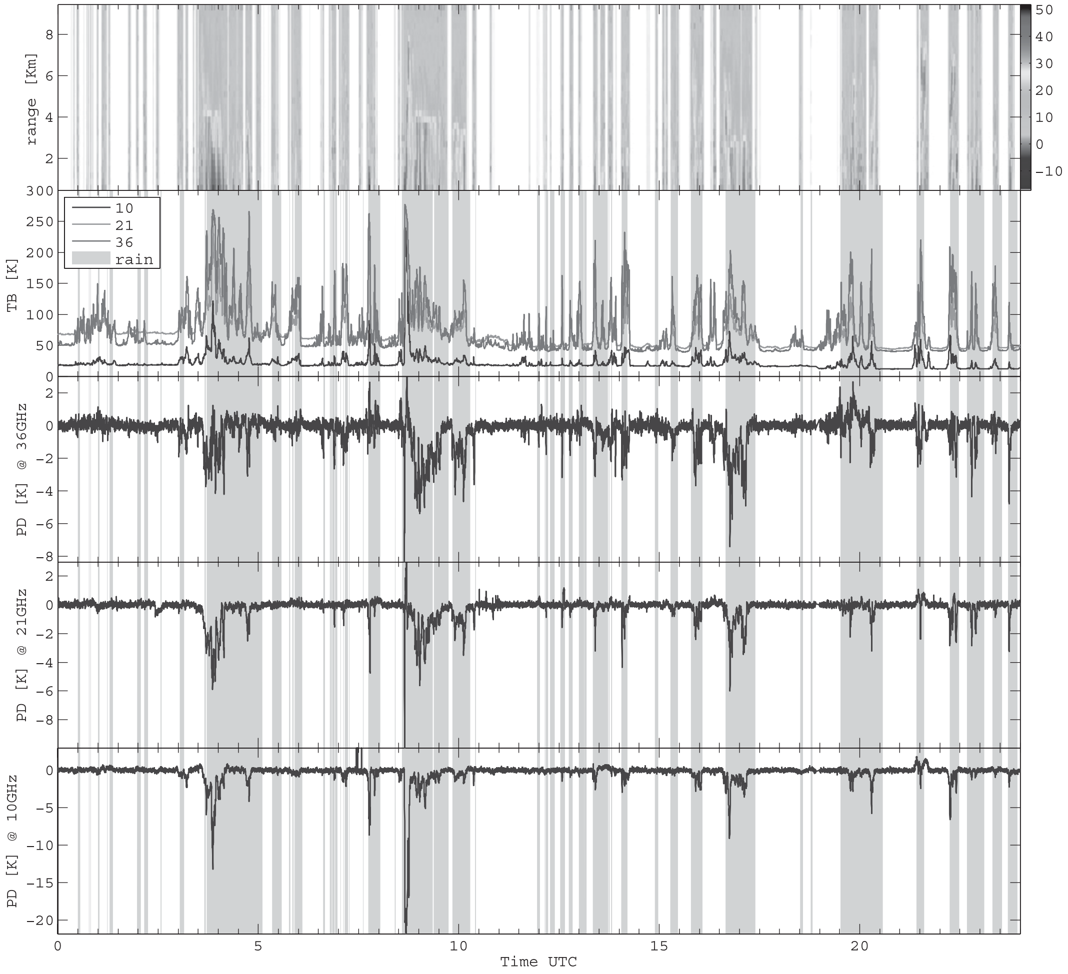

FIG. 3. ADMIRARI measurements during 1 Oct 2008. (top to bottom) MRR radar reflectivity (dB*Z*; vertical axis represents range along the slant path); ADMIRARI brightness temperatures [$T_B = 1/2(T_B^V + T_B^H)$]; and 36.5-, 21-, and 10.65-GHz polarization differences ($\mathrm{PD} = T_B^V - T_B^H$) at 30° elevation. Gray intervals indicate rainy periods as sensed by the rain sensor installed on the ADMIRARI trailer.

was improved by adding the rain shields and a 24-GHz micro rain radar (MRR) attached to the ADMIRARI's frame (black antenna on the right side of Fig. 1) and thus pointing at the same direction as the radiometer. Since the MRR beamwidth is 3°, the two instruments are looking approximately at the same slant volume.

In the frame of the EUCAARI campaign, ADMIRARI was deployed at the Cabauw Experimental Site for Atmospheric Research in the Netherlands and was continuously measuring from 6 May to 1 December 2008. A constant 30° elevation observation mode was adopted during the whole campaign. This observation mode will be the focus of the following sections.

The day of 1 October 2008 (Fig. 3) can be considered a golden day, with a variety of rain events both of stratiform and convective nature. The MRR reflectivity provides an immediate indication about the presence of rain along the slant path observed by the radiometer. Situations with quite different slant profiles were present during the day. The T_Bs [$T_B = 1/2(T_B^V + T_B^H)$] show a strong correlation with the reflectivity pattern—and thus the rain rate—(as expected) but with a frequency-dependent dynamic range: the 10-GHz channel does not exceed 240 K with a clear-sky baseline around 12 K, while 21-GHz (36.5 GHz) T_Bs range between 43 and 273 K (40 and 280 K). This is obviously due to the larger opacity of the atmosphere at higher frequencies. Exceptionally high T_Bs are reached around 0900 UTC.

The polarization differences are negative in presence of rain, in agreement with expectations. Extraordinary negative PD values correspond to the T_B peak at 10 GHz, while the two upper frequencies display positive PDs up to 3.5 K.

4. Model calculations: Spectral and polarization signatures of rainfall

The interaction of MW radiation with clouds and precipitation can be described by the vector radiative transfer equation (e.g., Haferman 2000), which can be solved with a range of methodologies (a review is provided by Mätzler 2006). Large atmospheric hydrometeors tend to have nonspherical shapes (e.g., falling raindrops, snow and other ice crystals) and preferential horizontal orientation. Therefore, hydrometeors represent dichroic media and polarization effects provide specific signatures. The polarization signal can be effectively used to distinguish between the rain and the cloud liquid water component of precipitating clouds.

The ADMIRARI's rationale is demonstrated in a simple scenario (Fig. 4). Similarly to Czekala et al. (2001b), we performed radiative transfer simulations by the fast polarized radiative transfer (RT4) code (Evans and Stephens 1991) in correspondence to the three ADMIRARI frequencies at an elevation angle of 30°. The computations are based on the 1D cloud resolving model hydrometeor profile (shown in Fig. 7). While preserving the vertical pattern, the amplitude of the cloud and rainwater content profiles has been modified in order to produce different combinations of c-LWP and r-LWP in a range of values from 0.0 to 5.0 kg m^{-2}. Raindrops are assumed to have a Marshall and Palmer drop size distribution (DSD). Three different isolines of constant LWP are depicted in Fig. 4: dashed lines indicate calculations with the same r-LWP but varying c-LWP, dash–dotted lines show the results for constant c-LWP, and dotted lines indicate the same total LWP. Pure cloud conditions are indicated by the uppermost horizontal dashed line (no-rain fraction). The increase in c-LWP from 0.0 to 5.0 kg m^{-2} leads to an increase in the corresponding T_B, but no polarization is produced. Pure rain conditions (in the absence of cloud) produce the lowest limit of the PD signal (indicated by the lowest dash–dotted line). When mixing rain into the cloud, increasing amounts of r-LWP shift the horizontal line of pure cloud response toward negative PDs.

The advantage of the PD additional information content in the partitioning of LWP is obvious. Let us consider a measurement of 155-K brightness temperature and −3.2-K polarization difference at 21 GHz identified by the cross of the horizontal and vertical dashed black lines in the bottom panel of Fig. 4. The T_B value of 155 K refers to 0.8 kg m^{-2} total liquid water path when assuming a composition of pure rain without clouds (retrieval case 1, pinpointed by the bottom arrow) or 3.1 kg m^{-2} c-LWP when assuming a pure cloud contribution (retrieval case 2, the top arrow). These numbers give a good estimate about the uncertainty in LWP retrieval in the presence of raining clouds with unknown cloud fraction when only T_B measurements are available. On the other hand, when the supplementary PD information is used (retrieval case 3, middle arrow in Fig. 4), a total LWP of 1.6 kg m^{-2} is estimated. Furthermore, we are now able to separate the total LWP in c-LWP (1.0 kg m^{-2}) and r-LWP (0.6 kg m^{-2}).

The importance of the ADMIRARI multispectral approach is immediately visible when looking at the Jacobians (Fig. 5), that is, at the sensitivity of the T_Bs and of the PDs depicted in Fig. 4 to c-LWP and r-LWP. In general the T_B sensitivity is much larger for the highest frequency (cf. the right with the left-center top and middle panels) and to rain (top versus middle panels). On the other hand, the benefit of the low frequency stems from the saturation of the signal at the higher frequencies. In the T_B-Jacobian plots (top and center panels in Fig. 5) 5 K $(\mathrm{kg\ m}^{-2})^{-1}$ can be considered as a boundary value. In fact, in regions with sensitivities below this value, an addition of 100 g m^{-2} would produce less than 0.5-K variation in the T_Bs. The 36.5-GHz channel loses sensitivity to rain (cloud) for profiles with r-LWP larger than 2.6 kg m^{-2} (1.8 kg m^{-2}). Conversely, the 10.6-GHz brightness temperatures are sensitive to rain and cloud almost everywhere. Similar considerations apply to the PD sensitivities (bottom panels in Fig. 5). Note that the PD-Jacobians can be either positive or negative. An addition of cloud water always damps the PDs (see the dashed isolines always slightly pointing upward in Fig. 4). The PD sensitivities to c-LWP (not shown) are indeed very small and they never exceed 0.5, 1.2, and 2.5 K $(\mathrm{kg\ m}^{-2})^{-1}$ at the three ADMIRARI frequencies, respectively. Conversely, an increase in the rain amount can produce either more negative PDs in the regime of small optical thicknesses (dash–dotted lines going downward) or more positive PDs in the regime of large optical thicknesses (dash–dotted lines going upward). The regions where the PDs are significantly responding to a change in r-LWP (bottom panels in Fig. 5) are reasonably estimated as those included within contour lines with absolute value larger than 3 K $(\mathrm{kg\ m}^{-2})^{-1}$.

The combination of scattering effects, the large spatial variation of precipitating hydrometeors in the atmosphere, and the finite beamwidth of the radiometers require the consideration of three-dimensional effects. Different techniques have been developed to numerically treat the radiative transfer equation for the full Stokes vector in a 3D environment in the presence of dichroic media (Haferman et al. 1993; Battaglia and Mantovani 2005; Davis et al. 2005). A recent comparison study (Battaglia et al. 2007) has demonstrated that,

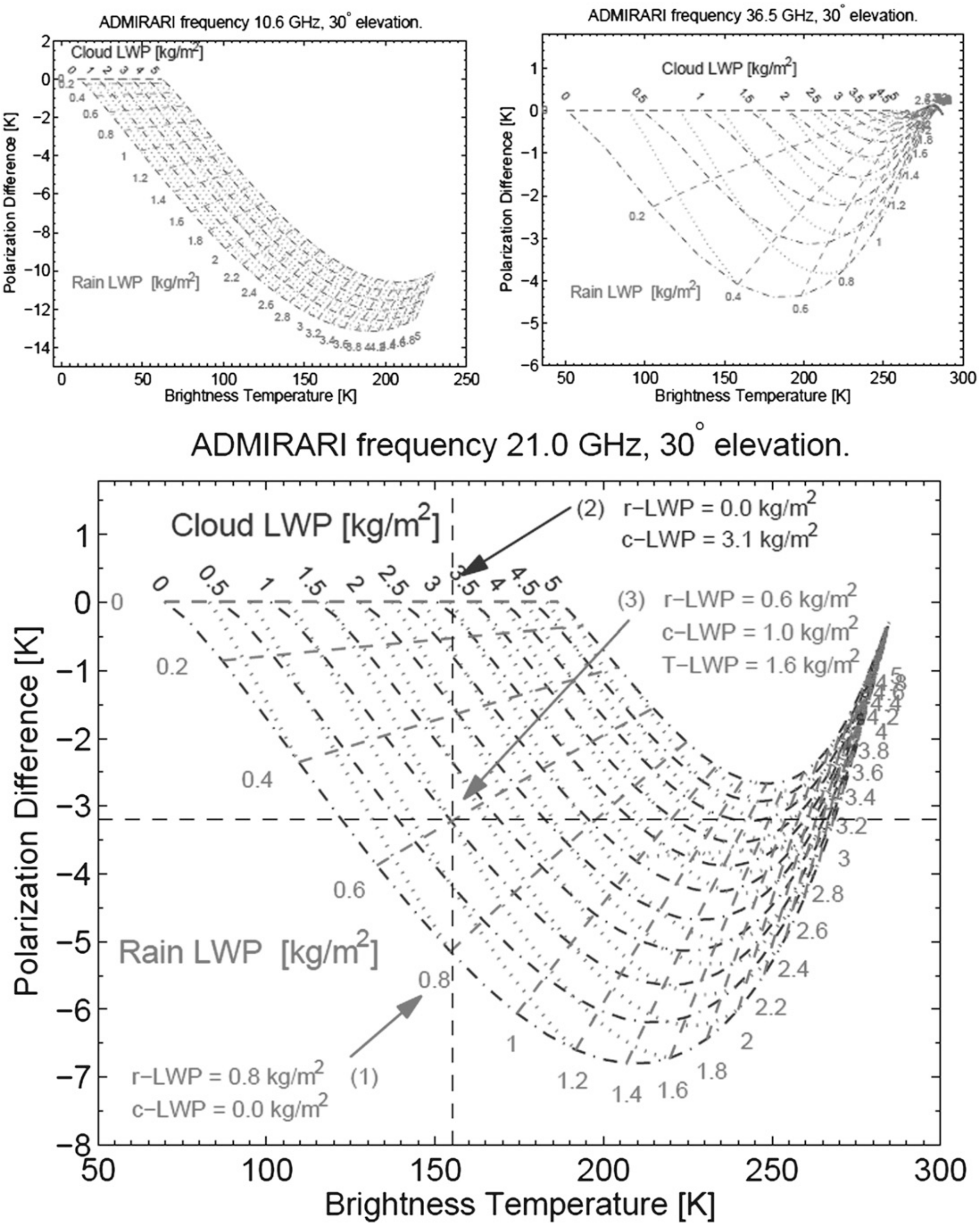

FIG. 4. Resulting PDs and T_Bs for different combinations of c-LWP and r-LWP at (top left) 10.6, (top right) 36.5, and (bottom) 21.0 GHz. A 30° elevation angle is assumed. Radiative transfer computations are based on the 1D cloud-resolving model hydrometeor profile shown in Fig. 7. While preserving the vertical profile shape, the amplitude of the cloud and rainwater content profiles is modified in order to produce the different combinations of c-LWP and r-LWP. Dashed lines indicate constant r-LWP, dash–dotted lines indicate constant c-LWP, and dotted lines indicate constant total LWP. (bottom) Three retrieval experiments (see text for details).

because of its lower computational cost, the backward–forward Monte Carlo technique based on importance sampling (Davis et al. 2005) represents the most efficient way to face passive microwave radiative transfer problems related to optically thick 3D structured clouds including nonspherical preferentially oriented hydrometeors. Therefore, the vector radiative transfer equation has been solved by a backward–forward Monte

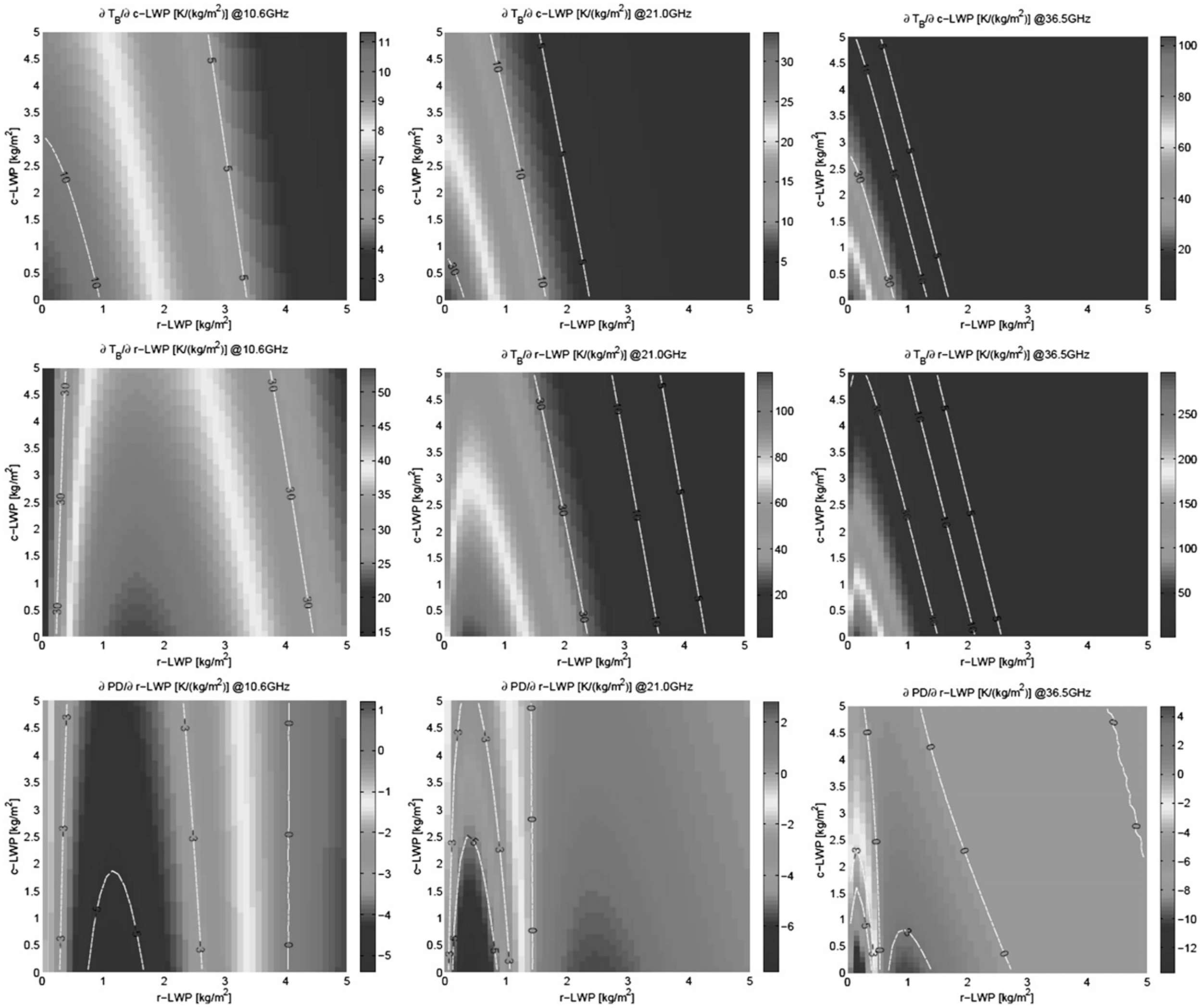

FIG. 5. Isolines of the Jacobians for T_Bs and PDs at (left) 10.6, (center) 21, and (right) 36.5 GHz, in correspondence to the same simulation of Fig. 4; (top) $\partial T_B/\partial r$ – LWP, (middle) $\partial T_B/\partial c$ – LWP, (bottom) $\partial PD/\partial r$ – LWP. All variables: K (kg m^{-2})$^{-1}$.

Carlo scheme, which can also easily account for a finite antenna beamwidth. This method represents a major step forward compared to former radiative transfer simulations of rain observations by ground-based radiometers, which always assumed plane parallel atmospheres with spherical hydrometeors and horizontal homogeneity (Sheppard 1996; Marzano et al. 2002, 2005a, 2006).

a. Box-type cloud model

To quantify the effects of the 3D structure of a raining cloud on the radiation field sensed by a polarimetric ground-based radiometer, the backward–forward method is applied to a box-type cloud model, as illustrated in Fig. 6. Here L_x and L_y are the horizontal dimensions of the rain shaft. The cloud-box profile is extracted from cloud-resolving model (CRM) simulations available from the Goddard Cumulus Ensemble (Tao and Simpson 1993; an example is shown in Fig. 7). Five hydrometeor types are included: rain, cloud water, cloud ice, graupel, and snow. Spherical raindrops are, however, replaced by mass-equivalent horizontally oriented oblate spheroids with axial ratios (lower than 1) parameterized according to Matrosov et al. (2002):

$$\mathcal{A} = 1.0 + 0.05b - bD_e \ (\text{cm}) \quad D_e > 0.05\ \text{cm}, \qquad (1)$$

as a function of the equivalent spherical raindrop diameter D_e. The shape factor b is equal to 0.6 for equilibrium drop shapes. The single-scattering properties (i.e., the extinction and the phase matrix and the emission vector) are computed with a T-matrix method according

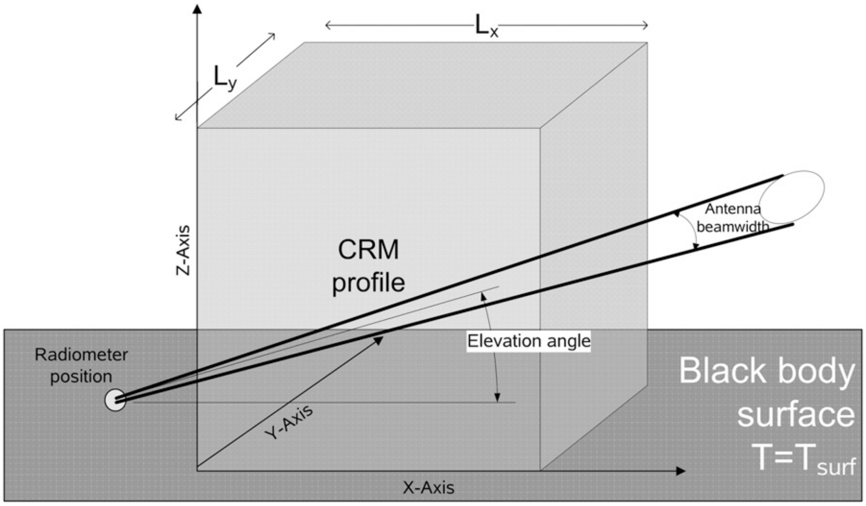

FIG. 6. Schematic for the rain cloud simulation. Radiances have been computed at observation points located at the location (P_x, P_y). The shaded area contains the rain system with one vertical hydrometeor and atmospheric profile extracted from a cloud-resolving model (like that shown in the Fig. 7). Nonshaded areas contain only atmospheric gases; temperature, pressure, and humidity profiles are the same as in the shaded area.

to Mishchenko (2000). The surface is assumed to be Lambertian with emissivity equal to 1.0. Assumption of surface emissivity equal to one may not be valid, especially for wet surfaces (e.g., Prigent et al. 2008). The emissivity effect is generally negligible for ADMIRARI measurements. In fact, changing surface emissivities from 1.0 to 0.8 (as expected for very wet surfaces) produces T_Bs (PDs) variations never larger than 1 K (0.2 K), that is, within the instrument measuring error. The emissivity impact is larger at intermediate T_Bs (150–200 K) and at higher frequencies, where the scattering signal is significantly and uniquely contributing to the total radiometer signal. In regimes where the downwelling radiation is dominated by emission processes (e.g., at small rain rates and low frequencies) or by blackbody-like response (e.g., at very high rain rates) the surface emissivity variability does not play any role. Cosmic radiation impinges at $T_c = 2.7$ K at the top of the atmosphere.

To include 3D effects each precipitating profile, characterized by different horizontal extents (varied from 250 to 8 km) is embedded in a clear-sky atmosphere (unshaded region in Fig. 6). The radiances are then simulated as sensed by a radiometer with an antenna beamwidth of 5° located at different positions either underneath the cloud or at the side of the cloud (the second option is depicted in Fig. 6). The radiative transfer equation is solved according to the backward Monte Carlo technique (Battaglia et al. 2007). The observation point is indicated by its coordinates (P_x, P_y). Simulated T_Bs and PDs are depicted in Fig. 8 based on the profile of Fig. 7 for a cloud box with $L_x = L_y = 4$ km, keeping P_x fixed at 0.75 km. Since the radiometer is sensitive to bulk-scattering properties within the whole beam, the rain effect can be sensed by the radiometer even from outside the rain shaft provided that it is operated at sufficiently slanted viewing angles. From pure geometric considerations, systems with altitude H are expected to affect the radiometric signal at distances $H/\tan\theta_{el}$, θ_{el} being the elevation angle (see Fig. 6). In the T_B plots shown in the right panels of Fig. 8, the homogeneous left upper parts represent regions which are still unaffected

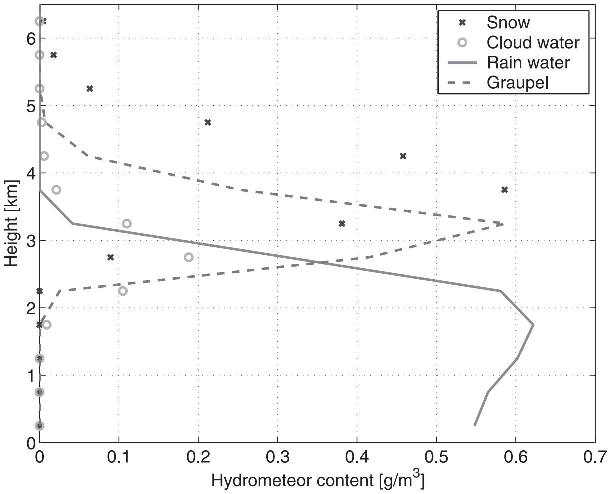

FIG. 7. Example of a hydrometeor profile extracted from a cloud-resolving model and adopted in the 3D radiative transfer simulations illustrated in Fig. 6.

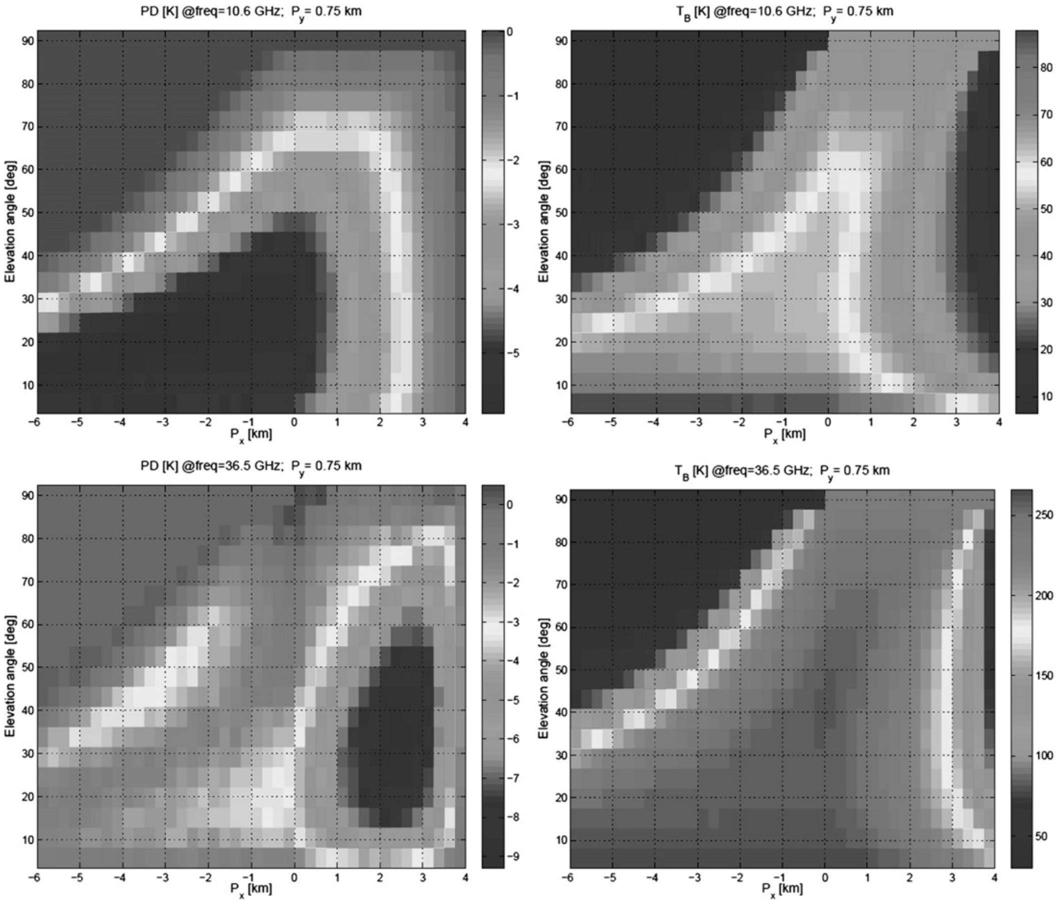

FIG. 8. (left) Polarization differences and (right) brightness temperatures simulated for the profile of Fig. 7 and the ground-based configuration depicted in Fig. 6 with $L_x = L_y = 4$ km. The (top) lowest and (bottom) highest ADMIRARI frequencies are considered.

by the rain shaft (where also the PDs are zero). On the other hand, even at 6-km distance the 10.6 GHz (36.5 GHz) is affected by the rain cell for elevation angles below 30° (40°), which translates to an altitude of 3.5 km (5.0 km). This agrees with the structure of the hydrometeor vertical profile shown in Fig. 7 (with the liquid phase confined below 3.5 km) and with the different sensitivity of the 10.6 and 36.5 GHz to the ice part of the cloud. Note that strongly negative PDs (e.g., left panels of Fig. 8) can be found for all three frequencies (but at different observing positions and elevation angles); on the other hand, slightly positive PDs are obtained only at the higher frequencies (see discussion of Fig. 9 later on).

b. Relevance of 3D effects

The relevance and role played by 3D effects in ground-based polarized radiometer observations were discussed in Battaglia et al. (2006). In the present study much more realistic profiles are included with vertical variability of hydrometeor profiles and with the presence of liquid water and ice particles. Three-dimensional effects are caused by geometrical and by scattering factors (Battaglia et al. 2005, and references therein). For scenarios with weak scattering, 3D effects are purely geometrical and the leakages from the radiatively warm side of the cloud can be accounted for by 1D slant-path (SP) approximation (Liu et al. 1996). As in section 5 of Battaglia et al. (2006), the relevance of "3D scattering effects" is evaluated by using as a reference 1D SP approximation calculations based on the fast RT4 code (Evans and Stephens 1991).

Differences between Monte Carlo and SP RT4 computations become noticeable at 21 GHz and even more at 36.5 GHz, as demonstrated in Fig. 9. Two striking features (see points bounded by ellipses) are evident: Monte Carlo produces more negative PDs in the region where the slant optical thickness is roughly around one (see discussion of Fig. 4 in Battaglia et al. 2006) and slightly positive PDs (up to 3.5 K at 36.5 GHz) when the

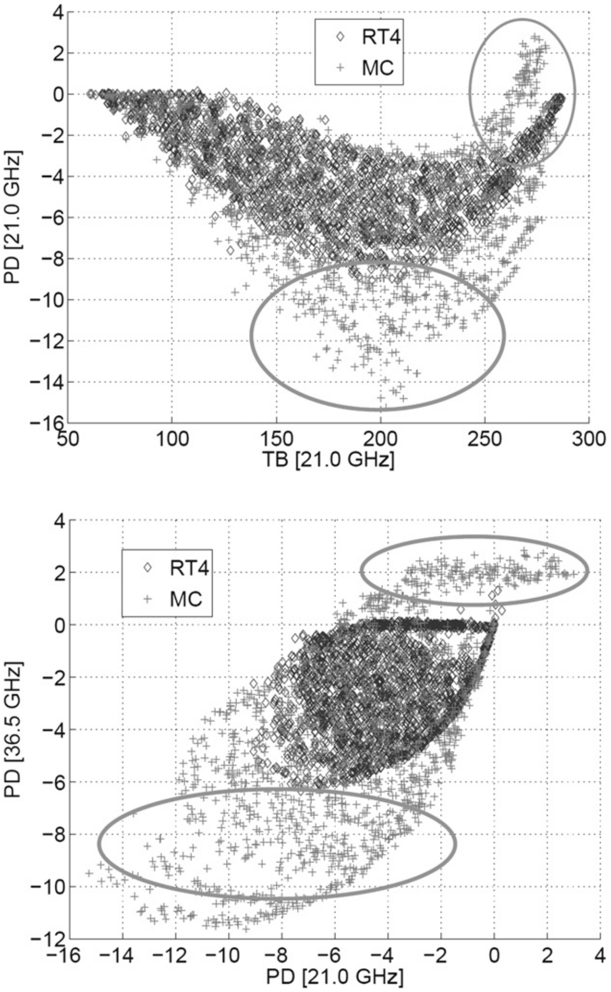

FIG. 9. Scatterplots between SP RT4 and Monte Carlo computations to highlight "3D scattering effects." The geometry of the simulations is the one illustrated in Fig. 6 with an elevation angle of 30°, $L_x = L_y = 4$ km and $P_x = (-3.5{:}1.0{:}3.5)$ km. About 3000 profiles with freezing levels ranging from 2 to 4 km are considered in this example: (top) PD vs T_B and (bottom) PD vs PD.

T_B signal is fully saturated (i.e., at large optical thicknesses). The SP RT4 cannot reproduce such large positive PDs at all. These discrepancies are attributable to the deficiencies of the 1D SP model in computing terms with orders of scattering ≥1. Conversely, at the lowest frequency, absorption represents the dominant process so that the predominant term affecting the total signal is the zeroth order of scattering, which is perfectly accounted for by the SP approximation (not shown).

c. *Sensitivity to axial ratio parameterizations and DSD assumptions*

Two factors are expected to play a crucial role in modifying the polarimetric radiometric signal: the axial ratio parameterizations and the DSD assumptions. Drop size distributions are usually modeled according to the exponential Marshall and Palmer distribution $N(D) = N_0 e^{-\Lambda D}$ with $N_0 = 8 \times 10^3$ m^{-3} mm^{-1}. The median volume diameter D_0 is approximately obtained as $D_0 = 3.67(r - \mathrm{LWC}/\pi\rho_w N_0)^{0.25}$, ρ_w being the density of water. To account for the departure from this shape, we consider hereinafter two other DSDs with $N_0 = 4 \times 10^3$ m^{-3} mm^{-1} (hereinafter referred as "thunderstorm") and $N_0 = 32 \times 10^3$ m^{-3} mm^{-1} ("drizzle"). This terminology follows the original paper by Joss and Waldvogel (1969) although the thunderstorm value here selected is more than twice as large. For the same amount of r-LWC, thunderstorm rain has a low number of raindrops with predominantly large diameter, while drizzles are characterized by a large amount of small droplets.

The parameterization of the axial ratio given in Eq. (1) is also modified by allowing variations of the shape factor b from 0.5 to 0.7, which accounts for the observed variability from the equilibrium value (Matrosov et al. 2002).

Modifications in the DSD assumptions affect the extinction properties of the medium and hence the T_Bs. This can be better understood by looking at the single particle extinction cross section of oblate raindrops (at 30° elevation) per unit volume (top panel of Fig. 10). This quantity exhibits a "super-Rayleigh behavior"; that is, it remains always higher than the corresponding diameter-independent Rayleigh value (which is identical to the value achieved at small diameters). In fact, in the Rayleigh approximation (e.g., for the cloud component), this quantity is expected to be equal to $6\pi/\lambda \mathrm{Im}(K)$ (about 0.018, 0.070, and 0.205 mm^{-1} for the three frequencies at 10°C), λ being the wavelength, $K \equiv m^2 - 1/m^2 + 2$ the dielectric factor, and m the complex refractive index of water. From a direct inspection of the top panel of Fig. 10 it is obvious that such an approximation is valid only for very small droplets with a decreasing range of applicability toward the higher frequencies. Moving out of the Rayleigh region on the left the three frequencies behave differently: while at 10.6 GHz the extinction per unit volume almost always increases with size, it reaches a maximum value around a diameter of 4 and 2.3 mm, at 21 and 36.5 GHz, respectively. When considering different DSDs (the amount of rainwater being the same), we can conclude that at 10.6 GHz DSDs containing large particles produce larger absorption and scattering coefficients (already noticed by Viltard et al. 2000 in their Fig. 2). But this is not always true at the other two frequencies (because of the nonmonotonic behavior of the extinction per unit volume curves in Fig. 10). This is highlighted in the bottom panel of Fig. 10, which depicts the V-pol extinction coefficients as a function of the

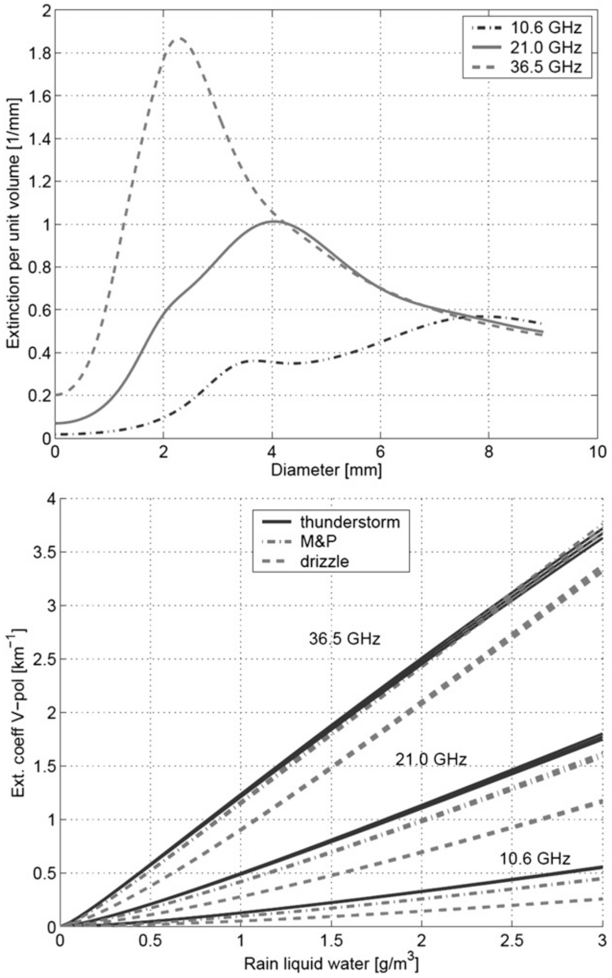

FIG. 10. (top) Extinction cross section per unit volume (mm^2 mm^{-3}) as a function of the raindrop equivolume diameter for the three ADMIRARI frequencies. Raindrops up to 9-mm diameter are considered. (bottom) Vertical polarization extinction coefficient as a function of the r-LWC (g m^{-3}) for raindrop populations with three different DSDs as indicated in the legend at the three ADMIRARI frequencies. The thickness of the line accounts for the assumed variability in the coefficient b in Eq. (1) from 0.5 to 0.7.

r-LWC: the thunderstorm DSDs, which favor large raindrops, produce the largest optical thicknesses (hence the highest T_Bs), except at 36.5 GHz at r-LWCs above 2.5 g m^{-3} where the M and P is actually the most efficient of the three DSDs in extinguishing radiation. Because of the large relative spread between the three DSDs visible in the bottom panel of Fig. 10, T_Bs at 10.6 GHz will be more heavily affected than at 36.5 GHz. Conversely, the axial ratio parameterization variability (in Fig. 10 indicated by the thickness of the line) is not expected to produce any appreciable variability in T_Bs. But it will play a key role in affecting the PDs (see below).

When considering PD effects, the larger the raindrops, the higher the dichroism of the medium, and the more negative the values attainable by the PDs will be. The same signal will be produced by more prolate raindrops (larger b values). While T_Bs are directly related to the extinction profiles, PDs are driven by other combinations of the scattering properties. Battaglia and Simmer (2007) showed that the following combination of scattering properties (k^{ext} and ϖ are the angular and polarization-dependent extinction coefficient and single-scattering albedo, respectively),

$$\Delta\xi(\theta_{\text{el}}) \equiv \frac{k_V^{\text{ext}}(\theta_{\text{el}})[1-\varpi_V(\theta_{\text{el}})] - k_H^{\text{ext}}(\theta_{\text{el}})[1-\varpi_H(\theta_{\text{el}})]}{0.5[k_V^{\text{ext}}(\theta_{\text{el}}) + k_H^{\text{ext}}(\theta_{\text{el}})]}, \tag{2}$$

is relevant when dealing with polarization differences driven by emission–absorption processes (as mainly happening at the ADMIRARI frequencies). As a rule of thumb, at small optical thicknesses, PDs are obtained by multiplying the parameter $\Delta\xi$ by the T_Bs. The parameter $\Delta\xi$ is plotted for $\theta_{\text{el}} = 30°$ in Fig. 11 as a function of r-LWC for the lowest and highest ADMIRARI frequency. The $\Delta\xi$ is always negative (hence negative PDs) and goes to zero at small r-LWC values (which produce DSDs with mainly spherical particles). The dynamic range attained at 10 GHz is much larger than at 36.5 GHz, which suggests the potential for reaching more negative PDs. A strong dependence on the b value is visible (curves with the same symbol are well separated): for instance a thunderstorm rain with a uniform r-LWC of 2.5 g m^{-3} producing a 10.6 GHz T_B equal to 100 K will roughly produce PD equal to −9.5, −11.5, and −14 K (see the three points in the top panel of Fig. 11). The same situation at 36.5 GHz will produce PDs less than half of these. While at 10 GHz DSDs with larger particles (given the same total amount of rain) always produce more negative PDs because of resonance effects, this is not valid any more at 36.5 GHz. At this frequency the most efficient DSDs are the thunderstorm, the M and P, and the drizzle roughly for r-LWC $<$ 0.5 g m^{-3}, 0.5 $<$ r-LWC $<$ 1.5 g m^{-3}, and r-LWC $>$ 1.5 g m^{-3}, respectively (see arrows in the bottom panel of Fig. 11).

These preliminary considerations have been tested with simulations performed following the methodology described in section 4a. Profiles with the same total hydrometeor content are hereafter considered; single-scattering properties have been computed by assigning the rain content to the three different DSDs and the b parameter to the three values (0.5, 0.6, 0.7). Results of the corresponding radiative transfer computations are shown in Fig. 12. Brightness temperatures (top panels of

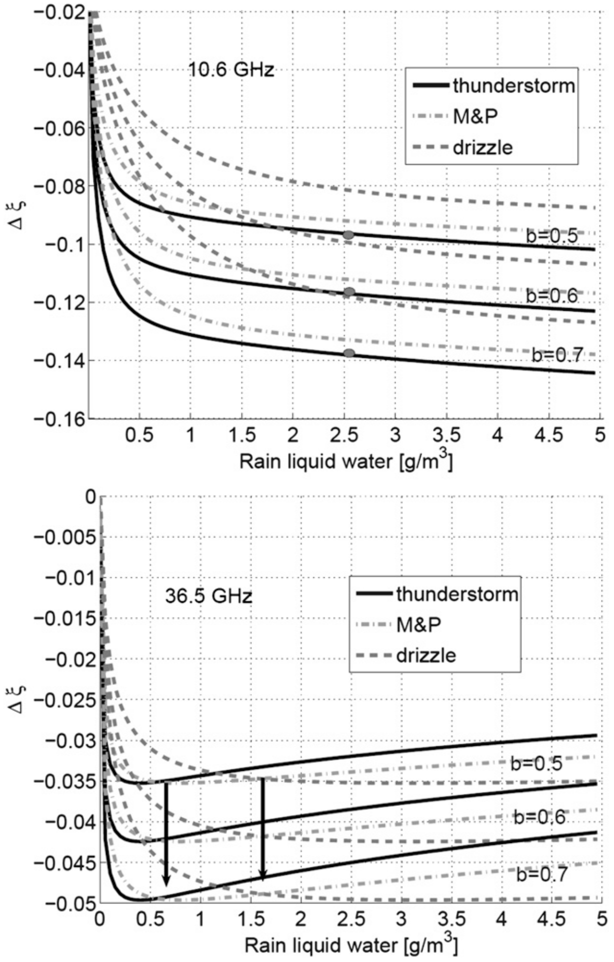

FIG. 11. Parameter $\Delta\xi$ as defined in Eq. (2) evaluated at elevation angle $\theta_{\mathrm{el}} = 30°$ at (top) 10.6 and (bottom) 36.5 GHz for three different DSD as a function of the r-LWC. Curves plotted with the same style correspond to different b values: (top to bottom) 0.5, 0.6, and 0.7. See text for details.

Fig. 12; the *M* and *P* DSD with $b = 0.6$ is taken as a reference) are unchanged by a change in the b value (the simulations with $b = 0.5$ and $b = 0.7$ with the *M* and *P* DSD coincide with the diagonal line), while they are significantly modified by the DSD assumption. The spread is more marked at 10 GHz than at the two highest frequencies and it can be as large as 70 K (see the double arrow in the top-left panel of Fig. 12). Note that, while at 10 GHz the thunderstorm DSD is always brighter than the other two, at 36.5 GHz when large T_Bs (>260 K) are encountered (and then, plausibly, large r-LWC as well) the drizzle type of rain becomes the brightest, which is expected from the previous discussion of the bottom panel of Fig. 10.

Polarization differences (middle panels of Fig. 12; the *M* and *P* DSD with $b_{\mathrm{eq}} = 0.6$ is taken again as a reference) are sensitive both to DSD and to the b parameters. The b dependence is roughly linear (cf. the curves labeled with $b = 0.5$ *M* and *P* and $b = 0.7$ *M* and *P* with the diagonal line). A change of ±0.1 in b produces a decrease/increase in PDs that scales linearly with PD:

$$\mathrm{PD}(b_{\mathrm{eq}} \pm 0.1) = \mathrm{PD}(b_{\mathrm{eq}})(1 \pm \eta_f), \tag{3}$$

with the correction factor η_f equal to about 18.5%, 17.5%, and 14.5%, respectively, for the three frequencies. For instance, at 10.6 GHz a PD = −10 K produced by assuming $b = 0.6$ will convert to −8.2 and −11.8 K when adopting $b = 0.5$ or $b = 0.7$, respectively. On the other hand, the effect of changing DSD is more subtle because the related change in T_Bs will alter the PDs themselves. This can be better understood by considering the T_B–PD space (bottom panels in Fig. 12). A change in the b factor in the range (0.5–0.7) will basically produce a pure up and down movement, whose intensity is indicated by the double arrows and will depend on the given PD level and on the frequency (see different length of the arrows). On the other hand a change in DSD will also produce a right–left shift; for example, a right movement when considering larger raindrops. If the absolute minimum of the T_B–PD curve is already reached, such a movement will push the solution toward a region where PDs actually decrease and therefore will not produce more negative values in the PDs. The bottom panels of Fig. 12 provide a clear picture about the uncertainties we have to contend with in the retrieval problem.

d. Relevance of melting layer effects

Melting hydrometeors are known to be brighter in terms of reflectivities and emissivities; that is, they have higher backscattering and extinction cross sections than equivolume raindrops. Battaglia et al. (2003) showed that the description of hydrometeor profiles without explicit use of mixed-phased hydrometeors generally underestimate the total optical thickness and the T_Bs. The effect is particularly strong when precipitating systems with low freezing levels are examined, and it is likely to affect the lower frequencies more (see Fig. 8 in Battaglia et al. 2003), that is, 10.6 GHz in our specific application. The shape of melting snowflakes has been parameterized, for example, by Russchenberg and Lighthart (1996) and Raynaud et al. (2000) in terms of oblate spheroids. These parameterizations, however, have not been verified in laboratory experiments so far. This represents a major obstacle for the current study since the axis ratio of melting ice particles drives the PD signal. Developing a model to assess the effect of the melting layer on the ADMIRARI signals is beyond the scope of this work and is left to future investigations.

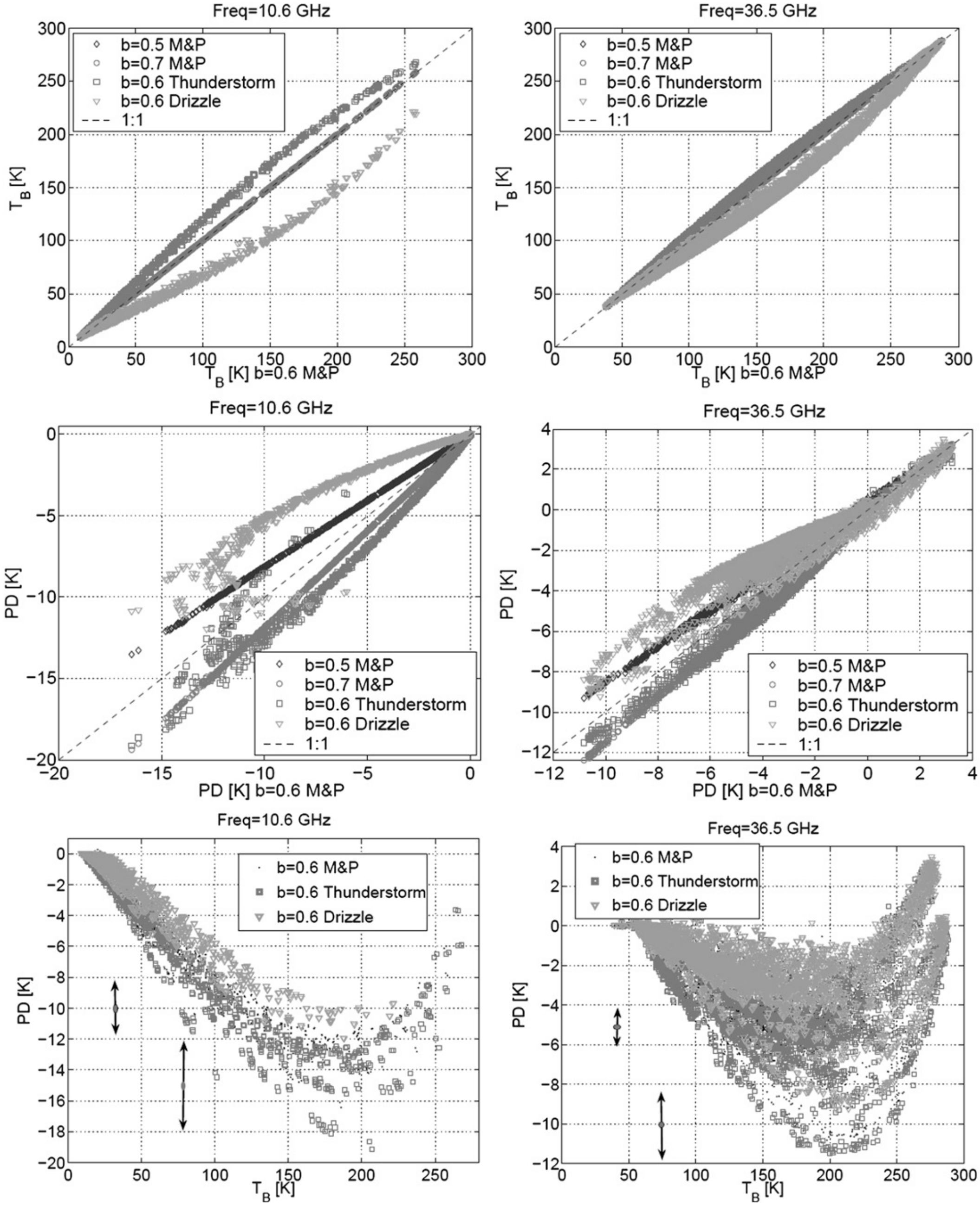

FIG. 12. Simulation study for the sensitivity of (top) T_Bs and (middle) PDs to the DSD and the assumed raindrops axial ratio [see Eq. (1)]. All panels take as reference the equilibrium axial ratio $b = 0.6$ and the Marshall–Palmer DSD. (bottom) Overall effect in the T_B–PD space. Only the (left) 10.6- and (right) 36.5-GHz ADMIRARI channels are here considered. See text for details.

5. Bayesian retrieval algorithm

Different techniques have been proposed to retrieve rain from ground-based radiometry. Marzano et al. (2002, 2005a, 2006) proposed, respectively, a variance-constrained regression, a principal component-based statistical, and a neural network retrieval algorithm for rain. Löhnert et al. (2004) presented a more physical direct retrieval for deriving physically consistent profiles of temperature, humidity, and cloud liquid water content by combining a suite of multi-instrument ground-based zenith observations. All measurements were integrated within the framework of optimal estimation to guarantee a retrieved profile with maximum information content.

Our retrieval technique of integrated water vapor IWV, cloud and rain liquid water path is based upon a Bayesian approach. The three-element vector $\boldsymbol{x}$ = (IWV, c-LWP, r-LWP) includes all the physical quantities to be retrieved in the inversion method while the vector $\mathbf{y}_{\text{obs}}$ represents the set of available sensor observations (i.e., a 6-element vector with the downwelling T_Bs and PDs at the three ADMIRARI frequencies). We use many realizations of the Goddard Cumulus Ensemble model to establish a prior probability density function of rainfall profiles (and of associated $\mathbf{x}_j$, $j = 1, \ldots, N_{\text{prof}}$, $N_{\text{prof}} \approx 10^6$). Detailed three-dimensional radiative transfer calculations (as described in section 4) are performed to determine the ADMIRARI simulated observations $\mathbf{y}_{\text{sim}}(\mathbf{x}_j)$ relative to the cloud model profiles. These simulations are intended to cover the regime with high rain rates where 3D effects are relevant; in addition to these, the database has been enriched by RT4 slant-path simulations in order to represent the regime of low and medium rain rates. Profiles without rain have been simulated by RT3 (Evans and Stephens 1991). For each CRM profile many different cloud thicknesses (L_x from 2 to 8 km) and positions (P_x from −6 to $L_x - 0.5$ km) are considered. It is assumed that the "best" estimate of $\mathbf{x}$, given the set of observations $\mathbf{y}_{\text{obs}}$, is the expected value

$$E(\mathbf{x}) = \int\int\ldots\int \mathbf{x}\,\text{pdf}(\mathbf{x})\,d\mathbf{x}, \tag{4}$$

where the probability density function pdf($\mathbf{x}$) is proportional to the conditional probability that $\mathbf{x}$ represents the true atmosphere state, $\mathbf{x}_{\text{true}}$, given that $\mathbf{y}$ is equal to the observed $\mathbf{y}_{\text{obs}}$. When using the large atmospheric profile–radiative database, an estimate of the expected value of Eq. (4) follows as (e.g., Kummerow et al. 1996)

$$\hat{E}(\mathbf{x}) = \sum_{j=1}^{N_{\text{prof}}} \mathbf{x}_j w_j, \quad \text{with} \tag{5}$$

$$w_j \equiv \frac{\exp\{-0.5[\mathbf{y}_{\text{obs}} - \mathbf{y}_{\text{sim}}(\mathbf{x}_j)]^{\text{T}}(\mathcal{O}+\mathcal{S})^{-1}[\mathbf{y}_{\text{obs}} - \mathbf{y}_{\text{sim}}(\mathbf{x}_j)]\}}{\sum_{k=1}^{N_{\text{prof}}} \exp\{-0.5[\mathbf{y}_{\text{obs}} - \mathbf{y}_{\text{sim}}(\mathbf{x}_k)]^{\text{T}}(\mathcal{O}+\mathcal{S})^{-1}[\mathbf{y}_{\text{obs}} - \mathbf{y}_{\text{sim}}(\mathbf{x}_k)]\}},$$

where the summation is carried over all model simulated profiles ($\mathbf{x}_j$) in the atmosphere/radiative model database. In Eq. (5) $\mathcal{O}$ and $\mathcal{S}$ are the observation and model error covariance matrices, respectively, which are assumed to be diagonal with $\sigma_{\mathcal{O}}(T_B) = 1\,\text{K}$ and $\sigma_{\mathcal{O}}(\text{PD}) = 0.5\,\text{K}$ and with $\sigma_{\mathcal{S}}(T_B) = 1\,\text{K}$ and $\sigma_{\mathcal{S}}(\text{PD}) = (\eta_f/3)|\text{PD}|\,\text{K}$ following the uncertainties related to the shape factor; see Eq. (3). We introduce also a quality index (QI) for assessing the quality of the matching between simulations and observations defined as

$$\text{QI} \equiv \min\{[\mathbf{y}_{\text{obs}} - \mathbf{y}_{\text{sim}}(\mathbf{x}_j)]^{\text{T}}(\mathcal{O}+\mathcal{S})^{-1}[\mathbf{y}_{\text{obs}} - \mathbf{y}_{\text{sim}}(\mathbf{x}_j)]\}, \tag{6}$$

where the minimum is searched over the whole database of simulated profiles. Values of QI lower than 6 indicate that we are fitting all six measurements on average within the model/measurement standard deviation. Values larger than 15–20 indicate a bad agreement between measurements and simulations.

Parallel to the ADMIRARI retrieval we performed a completely independent retrieval for the r-LWP based only on the MRR measurements. Assuming the validity of Rayleigh approximation for the reflectivity and an exponential DSD, the relationship between radar reflectivity and r-LWC is provided by

$$r - \text{LWC}\,(\text{g m}^{-3}) = 7.32e - 05 \times [N_0\,(\text{m}^{-3}\,\text{mm}^{-1})]^{0.4286} \times [Z\,(\text{mm}^6\,\text{m}^{-3})]^{0.5714}, \tag{7}$$

which can be integrated over the whole MRR slant path located below the freezing level to get the slant r-LWP. In the following we use the Marshall and Palmer value $N_0 = 8 \times 10^3\ \text{m}^{-3}\ \text{mm}^{-1}$ in Eq. (7). The variability of N_0 as introduced in section 4c already accounts for a variation of −25% and +80% with respect to this selected value. Because the MRR is operated in slant condition the usual attenuation correction based on the Doppler spectrum at each level is not feasible. A pure reflectivity-based attenuation correction is extremely instable; thus, it has been avoided.

An example of the retrieval results for observations collected in the afternoon of 30 September 2008 is provided in Fig. 13. Humidity and temperature conditions can be described by an IWV around 25 kg m^{-2}, a surface temperature around 10°C, and a freezing level located close to 2-km height. A continuous rain event starting just before 1800 UTC is here considered. The event is highlighted by negative PDs at all frequencies (top right panel of Fig. 13) and by high MRR reflectivities (middle right panel of Fig. 13). The QI (middle-left panel of Fig. 13) shows values almost always lower

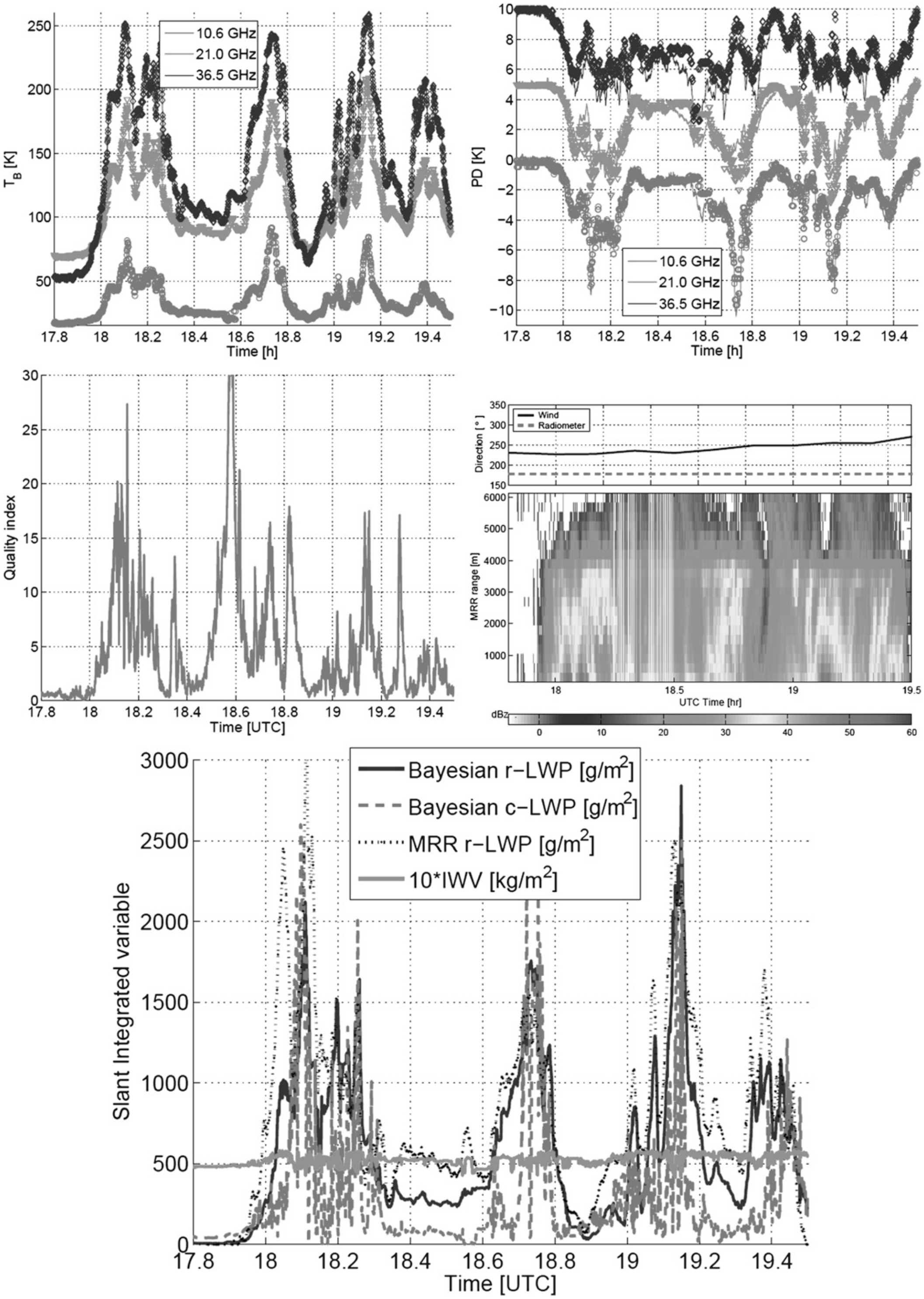

FIG. 13. Case study 30 Sep 2008 from 17.8 to 19.4 h. (top left) Radiometer T_Bs. (top right) PDs with an offset of 0, +5, and +10 K for the 10-, 21-, and 36-GHz channels, respectively. (middle left) Retrieval quality index. (middle right) MRR reflectivity including (on top) the wind (black line) and radiometer observation (dashed line) directions. (bottom) IWV and rain and cloud LWP retrieved.

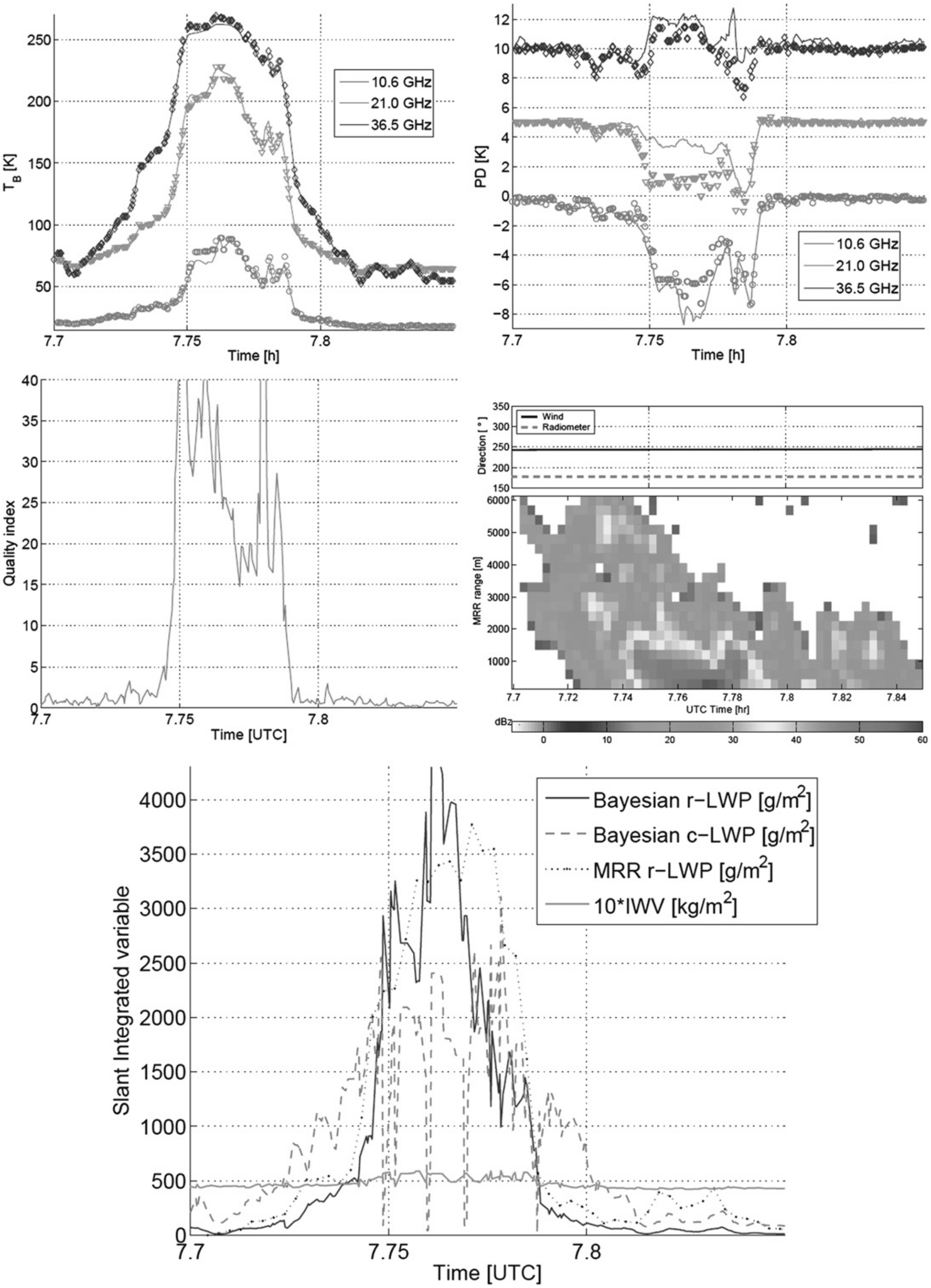

FIG. 14. As in Fig. 13, for the case study 1 Oct 2008 from 7.7 to 7.8 h.

than 15, that is, low residuals, indicating that the simulations generally fit the observations. This is also demonstrated in the top panels of Fig. 13 where the measured (continuous line) and closest-to-measured simulated (diamonds) T_Bs and PDs are shown. It is important to note that these observations do not show any evidence of water remaining on the sensor after each rain spell. This fact is confirmed by the sharp T_B transitions from rainy to not-rainy spells and, therefore, by the absence of a recovery period needed for drying the antenna [as is, on the other hand, evident in the observations of Fig. 7 in Marzano et al. (2005b)]. As an indirect proof of that, we plotted the wind vector direction and the radiometer viewing direction in the middle-right panel of Fig. 13. The vicinity of the two enhances our confidence of having dry antennas during the whole event.

When reverting to the retrieval products (bottom panel of Fig. 13) there is a quite reasonable agreement between the 10-s averaged ADMIRARI Bayesian retrieved slant r-LWP (continuous line) and the 10-s MRR Z-based slant r-LWP (dotted black line). Since the elevation angle of our observation is 30°, it suffices to divide by 2 our slant quantities in order to obtain an equivalent zenith LWP. The mismatch between the two curves is certainly compatible with the high uncertainty related to the MRR retrieval, mainly because of the absence of an attenuation correction and to the strong sensitivity to the DSD assumption. In addition, given the extremely high temporal resolution of the product (10 s) the imperfect matching between the sampled volumes (the MRR has a beamwidth of 3° only) can play a role as well. Nevertheless, based on several rain events, we found a correlation coefficient and a RMS between ADMIRARI-retrieved r-LWP and MRR-based r-LWP of 0.77 and 0.38 kg m^{-2}, respectively.

The panels in Fig. 14 depict a short ($\approx$10 min) strong convective event. In this case slant r-LWP and c-LWP higher than 4 and 2.5 kg m^{-2} are retrieved by the algorithm. Note how the onset and the end of the precipitation period (clearly evident in the MRR image) are well captured by the radiometer as well. Close to the peak of r-LWP the QI becomes extremely poor. We have to remark that we found a downward misalignment of the 10.6 GHz antenna relative to the other two antennas by 7°. Although this has been accounted for in the retrieval scheme, the mismatch between the slant volume observed by the three channel adds additional uncertainty. For this specific case the cloud retrieval looks quite instable in the region of high QIs, with sharp oscillations. This is thought to be an artifact of the retrieval more than a real cloud feature. Note that this alignment problem explains also the mismatch between the simulated and observed T_Bs during the COPS campaign mentioned in Battaglia et al. (2009).

6. Conclusions and future work

The new-concept multiwavelength dual-polarized ADMIRARI has been presented. Its main advantage is represented by its capability of being operated in rainy conditions and of retrieving simultaneously water vapor, rain, and cloud liquid water paths. Specifics and characteristics of the sensor together with the Bayesian retrieval scheme and the inherent 3D radiative transfer simulations have been described in detail. Extensive observations show that observed brightness temperatures and polarization differences can be well interpreted and reproduced by simulated ones for all three channels simultaneously. Rough estimates of r-LWP derived from collocated observations with a micro rain radar seem to confirm the rain/no-rain separation and the variability trend of r-LWP provided by the radiometer-based retrieval algorithm.

Future work envisions applying the retrieval scheme to all our measurement databases in order to produce climatological information about the rain/cloud partitioning for midlatitude precipitation systems; this will provide groundbreaking feedbacks for cloud modelers toward a better characterization of rain processes. An improved synergy between our radiometer and the MRR is also foreseen via the integration of the range-resolved radar information directly in the retrieval procedure. Dedicated studies to well-defined stratiform cases should better characterize the brightband extinction enhancements at the ADMIRARI frequencies, with immediate repercussions in spaceborne radiometry application. ADMIRARI is scheduled to participate to upcoming NASA Global Precipitation Mission ground-validation campaigns (e.g., in Finland in 2010 and in Oklahoma in 2011). This will offer better opportunities to validate the r-LWP and c-LWP partitioning by independent observations provided by polarimetric radars and/or multiwavelength scanning radar observations (like those foreseen at the Oklahoma Atmospheric Radiation Measurement Program site).

Acknowledgments. The ADMIRARI radiometer and this research have been funded by the Deutsche Forschungsgemeinschaft (DFG) under Grant BA 3485/1-1. The authors thank the Cabauw site for hosting ADMIRARI during the EUCAARI campaign. The authors are grateful to F. Evans for making the RT3 and RT4 software available at the Web site http://nit.colorado.edu/polrad.html. We also acknowledge the very helpful and detailed remarks of the anonymous reviewers, who considerably improved on the readability of the text.

REFERENCES

Andsager, K., K. V. Beard, and N. S. Laird, 1999: A laboratory study of oscillations and axis ratios for large raindrops. *J. Atmos. Sci.,* **56,** 2673–2683.

Battaglia, A., and S. Mantovani, 2005: Forward Monte Carlo computations of fully polarized microwave radiation in non isotropic media. *J. Quant. Spectrosc. Radiat. Transfer,* **95,** 285–308.

——, and C. Simmer, 2007: Explaining the polarization signal from rain dichroic effects. *J. Quant. Spectrosc. Radiat. Transfer,* **105,** 84–101, doi:10.1016/j.jqsrt.2006.11.012.

——, C. Kummerow, D.-B. Shin, and C. Williams, 2003: Toward characterizing the effect of radar bright bands on microwave brightness temperatures. *J. Atmos. Oceanic Technol.,* **20,** 856–871.

——, F. Prodi, F. Porcu, and D.-B. Shin, 2005: 3D effects in microwave radiative transport inside precipitating clouds: Modeling and applications. *Measuring Precipitation from Space: EURAINSAT and the Future,* V. Levizzani, P. Bauer, and F. J. Turk, Eds., Springer, 113–125.

——, H. Czekala, and C. Simmer, 2006: Three-dimensional effects in polarization signatures as observed from precipitating clouds by low frequency ground-based microwave radiometers. *Atmos. Chem. Phys.,* **6,** 4383–4394.

——, C. Davis, C. Emde, and C. Simmer, 2007: Microwave radiative transfer intercomparison study for 3-D dichroic media. *J. Quant. Spectrosc. Radiat. Transfer,* **105,** 55–67, doi:10.1016/j.jqsrt.2006.09.017.

——, P. Saavedra, T. Rose, and C. Simmer, 2009: Rain observations by a multi-frequency dual polarized radiometer. *IEEE Geosci. Remote Sens. Lett.,* **6,** 354–358.

Chuang, C., and K. V. Beard, 1990: A numerical model for the equilibrium shape of electrified raindrops. *J. Atmos. Sci.,* **47,** 1374–1389.

Crewell, S., and U. Löhnert, 2003: Accuracy of cloud liquid water path from ground-based microwave radiometry 2. Sensor accuracy and synergy. *Radio Sci.,* **38,** 8042, doi:10.1029/2002RS002634.

——, H. Czekala, U. Löhnert, C. Simmer, T. Rose, and R. Zimmermann, 2001: MICCY-a 22 channel ground-based microwave radiometer for atmospheric research. *Radio Sci.,* **36,** 621–638.

Czekala, H., and C. Simmer, 1998: Microwave radiative transfer with nonspherical precipitating hydrometeors. *J. Quant. Spectrosc. Radiat. Transfer,* **60,** 365–374.

——, and ——, 2002: On precipitation induced polarization of microwave radiation measured from space. *Meteor. Z.,* **11,** 49–60.

——, S. Crewell, A. Hornbostel, A. Schroth, C. Simmer, and A. Thiele, 2001a: Interpretation of polarization features in ground based microwave observations as caused by horizontally aligned oblate rain drops. *J. Appl. Meteor.,* **40,** 1918–1932.

——, ——, C. Simmer, and A. Thiele, 2001b: Discrimination of cloud and rain liquid water path by groundbased polarized microwave radiometry. *Geophys. Res. Lett.,* **28,** 267–270.

Davis, C. P., C. Emde, and R. S. Harwood, 2005: A 3D polarized reversed Monte Carlo radiative transfer model for mm and sub-mm passive remote sensing in cloudy atmospheres. *IEEE Trans. Geosci. Remote Sens.,* **43,** 1096–1101.

Evans, K. F., and G. L. Stephens, 1991: A new polarized atmospheric radiative transfer model. *J. Quant. Spectrosc. Radiat. Transfer,* **46,** 413–423.

Haferman, J. L., 2000: Microwave scattering by precipitation. *Light Scattering by Nonspherical Particles: Theory, Measurements, and Applications,* M. I. Mishchenko, J. W. Hovenier, and L. D. Travis, Eds., Academic Press, 482–524.

——, W. F. Krajewski, T. F. Smith, and A. Sanchez, 1993: Radiative transfer for a three-dimensional raining cloud. *Appl. Opt.,* **32,** 2795–2802.

Jacobson, M., and W. Nunnelee, 1997: Design and performance of a spinning flat reflector for millimeter-wave radiometry. *IEEE Trans. Geosci. Remote Sens.,* **35,** 464–466.

——, D. Hogg, and J. Snider, 1986: Wet reflectors in millimeter-wave radiometry-experiment and theory. *IEEE Trans. Geosci. Remote Sens.,* **24,** 784–791.

Janssen, M. A., Ed., 1996: *Atmospheric Remote Sensing by Microwave Radiometry.* John Wiley & Sons, 572 pp.

Joss, J., and A. Waldvogel, 1969: Raindrop size distribution and sampling size errors. *J. Atmos. Sci.,* **26,** 566–569.

Kummerow, C., W. S. Olson, and L. Giglio, 1996: A simplified scheme for obtaining precipitation and vertical hydrometeor profiles from passive microwave sensors. *IEEE Trans. Geosci. Remote Sens.,* **34,** 1213–1232.

Kutuza, B. G., G. K. Zagorin, A. Hornbostel, and A. Schroth, 1998: Physical modeling of passive polarimetric microwave observations of the atmosphere with respect to the third stokes parameter. *Radio Sci.,* **33,** 677–695.

Liljegren, J. C., E. E. Clothiaux, G. G. Mace, S. Kato, and X. Dong, 2001: A new retrieval for cloud liquid water path using a ground-based microwave radiometer and measurements of cloud temperature. *J. Geophys. Res.,* **106** (D13), 14 485–14 500.

Liu, G.-R., C.-C. Liu, and T.-H. Kuo, 2001: Rainfall intensity estimation by ground-based dual frequency microwave radiometers. *J. Appl. Meteor.,* **40,** 1035–1041.

Liu, Q., and C. Simmer, 1996: Polarization and intensity in microwave radiative transfer. *Beitr. Phys. Atmos.,* **69,** 535–545.

——, ——, and E. Ruprecht, 1996: Three-dimensional radiative transfer effects of clouds in the microwave spectral range. *J. Geophys. Res.,* **101** (D2), 4289–4298.

Löhnert, U., and S. Crewell, 2003: Accuracy of cloud liquid water path from ground-based microwave radiometry 1. Dependency on cloud model statistics. *Radio Sci.,* **38,** 8041, doi:10.1029/2002RS002654.

——, ——, and C. Simmer, 2004: An integrated approach towards retrieving physically consistent profiles of temperature, humidity and cloud liquid water. *J. Appl. Meteor.,* **43,** 1295–1307.

——, ——, O. Krasnov, E. O'Connor, and H. Russchenberg, 2008: Advances in continuously profiling the thermodynamic state of the boundary layer: Integration of measurements and methods. *J. Atmos. Oceanic Technol.,* **25,** 1251–1266.

——, D. Turner, and S. Crewell, 2009: Ground-based temperature and humidity profiling using spectral infrared and microwave observations. Part I: Simulated retrieval performance in clear-sky conditions. *J. Appl. Meteor. Climatol.,* **48,** 1017–1032.

Marzano, F. S., E. Fionda, P. Ciotti, and A. Martellucci, 2002: Ground-based multi-frequency microwave radiometry for rainfall remote sensing. *IEEE Trans. Geosci. Remote Sens.,* **40,** 742–759.

——, D. Cimini, P. Ciotti, and R. Ware, 2005a: Modeling and measurements of rainfall by ground-based multispectral microwave radiometry. *IEEE Trans. Geosci. Remote Sens.,* **43,** 1000–1011.

——, ——, and R. Ware, 2005b: Monitoring of rainfall by ground-based passive microwave systems: Models, measurements and applications. *Adv. Geosci.,* **2,** 259–265.

——, E. Fionda, and P. Ciotti, 2006: Neural-network approach to ground-based passive microwave estimation of precipitation intensity and extinction. *J. Hydrol.,* **328,** 121–131.

Matrosov, S., K. Clark, B. Martner, and A. Tokay, 2002: X-band polarimetric radar measurements of rainfall. *J. Appl. Meteor.,* **41,** 941–952.

Mätzler, C., 2006: *Thermal Microwave Radiation: Applications for Remote Sensing*. Institution of Engineering and Technology, 584 pp.

——, and J. Morland, 2008: Advances in surface-based radiometry of atmospheric water. Universität Bern Institut für angewandte Physik Research Rep. 2008-02-MW, 51 pp.

Mishchenko, M. I., 2000: Calculation of the amplitude matrix for a nonspherical particle in a fixed orientation. *Appl. Opt.,* **39,** 1026–1031.

Prigent, C., E. Jaumouillé, F. Chevallier, and F. Aires, 2008: A parameterization of the microwave land surface emissivity between 19 and 100 GHz, anchored to satellite-derived estimates. *IEEE Trans. Geosci. Remote Sens.,* **46,** 344–352.

Pujol, O., J.-F. Georgis, L. Feral, and H. Sauvageot, 2007: Degradation of radar reflectivity by cloud attenuation at microwave frequency. *J. Atmos. Oceanic Technol.,* **24,** 640–657.

Raynaud, L., I. Chenerie, and J. Lemorton, 2000: Modeling of radiowave scattering in the melting layer of precipitation. *IEEE Trans. Geosci. Remote Sens.,* **38,** 1574–1584.

Rose, T., S. Crewell, U. Löhnert, and C. Simmer, 2005: A network suitable microwave radiometer for operational monitoring of the cloudy atmosphere. *Atmos. Res.,* **75,** 183–200, doi:10.1016/j.atmosres.2004.12.005.

Russchenberg, H., and L. Lighthart, 1996: Backscattering by and propagation through the melting layer of precipitation: A new polarimetric model. *IEEE Trans. Geosci. Remote Sens.,* **34,** 3–14.

Sheppard, B., 1996: Effect of rain on ground-based microwave radiometric measurements in the 20–90-GHz range. *J. Atmos. Oceanic Technol.,* **13,** 1139–1151.

Solheim, F., J. R. Godwin, E. R. Westwater, Y. Han, S. J. Keihm, K. Marsh, and R. Ware, 1998: Radiometric profiling of temperature, water vapor and cloud liquid water using various inversion methods. *Radio Sci.,* **33,** 393–404.

Tao, W. K., and J. Simpson, 1993: Goddard cumulus ensemble model. Part I: Model description. *Terr. Atmos. Oceanic Sci.,* **4,** 35–72.

Troitsky, A. V., A. M. Osharin, A. V. Korolev, and J. W. Strapp, 2003: Polarization of thermal microwave atmospheric radiation due to scattering by ice particles in clouds. *J. Atmos. Sci.,* **60,** 1608–1620.

Viltard, N., C. D. Kummerow, W. S. Olson, and Y. Hong, 2000: Combined use of the radar and radiometer of TRMM to estimate the influence of drop size distribution on rain retrievals. *J. Appl. Meteor.,* **39,** 2103–2114.

Westwater, E. R., 1978: The accuracy of water vapor and cloud liquid determination by dual-frequency ground-based microwave radiometry. *Radio Sci.,* **13,** 667–685.

——, S. Crewell, and C. Mätzler, 2004: A review of surface-based microwave and millimeter-wave radiometric remote sensing of the troposphere. *Radio Sci. Bull.,* **310,** 59–80.

Wulfmeyer, V., and Coauthors, 2008: Research campaign: The convective and orographically induced precipitation study. *Bull. Amer. Meteor. Soc.,* **89,** 1477–1486.